Received: 29 July 2021 | Revised: 4 November 2021 | Accepted: 12 November 2021

DOI: 10.1002/mrm.29108

RESEARCH ARTICLE

Magnetic Resonance in Medicine

Velocity vector reconstruction for real-time phase-contrast MRI with radial Maxwell correction

Jost M. Kollmeier | **Oleksandr Kalentev** | **Jakob Klosowski** | **Dirk Voit** | **Jens Frahm**

Biomedizinische NMR, Max-Planck-Institut für biophysikalische Chemie, Göttingen, Germany

Correspondence
Jost M. Kollmeier, Biomedizinische NMR, Max-Planck-Institut für biophysikalische Chemie, 37070 Göttingen, Germany.
Email: jost.kollmeier@mpibpc.mpg.de

Purpose: To develop an auto-calibrated image reconstruction for highly accelerated multi-directional phase-contrast (PC) MRI that compensates for (1) reconstruction instabilities occurring for phase differences near $\pm\pi$ and (2) phase errors by concomitant magnetic fields that differ for individual radial spokes.

Theory and Methods: A model-based image reconstruction for real-time PC MRI based on nonlinear inversion is extended to multi-directional flow by exploiting multiple flow-encodings for the estimation of velocity vectors. An initial smoothing constraint during iterative optimization is introduced to resolve the ambiguity of the solution space by penalizing phase wraps. Maxwell terms are considered as part of the signal model on a line-by-line basis to address phase errors by concomitant magnetic fields. The reconstruction methods are evaluated using simulated data and cross-sectional imaging of a rotating-disc, as well as in vivo for the aortic arch and cervical spinal canal at 3T.

Results: Real-time three-directional velocity mapping in the aortic arch is achieved at $1.8 \times 1.8 \times 6$ mm^3 spatial and 60 ms temporal resolution. Artificial phase wraps are avoided in all cases using the smoothness constraint. Inter-spoke differences of concomitant magnetic fields are effectively compensated for by the model-based image reconstruction with integrated radial Maxwell correction.

Conclusion: Velocity vector reconstructions based on nonlinear inversion allow for high degrees of radial data undersampling paving the way for multi-directional PC MRI in real time. Whether a spoke-wise treatment of Maxwell terms is required or a computationally cheaper frame-wise approach depends on the individual application.

KEYWORDS

concomitant fields, Maxwell correction, model-based reconstruction, nonlinear inverse reconstruction, phase-contrast, radial MRI, real-time MRI, velocity vector

1 | INTRODUCTION

Phase-contrast (PC) MRI is a valuable tool for the quantitative assessment of flow velocities with the potential to measure velocities in multiple directions. Its main drawback, however, is a poor scan efficiency when using traditional PC MRI methods resulting in limited temporal resolution or long total acquisition times. More recent variants benefit from efficient acquisition strategies and advanced image reconstruction techniques that even allow for real-time PC MRI,[1] i.e., imaging without physiological gating or retrospective data sorting. Exemplary implementations exploit spiral sampling,[2–4] echo-planar trajectories,[5,6] low-rank constraints,[7] or radial acquisitions.[8–10] While these real-time techniques concentrate on one-directional through-plane flow only (2D PC MRI), in-plane flow components are neglected as additional flow directions demand additional measurements compromising temporal resolution.

Recently, an extension of real-time velocity mapping to multiple directions was proven feasible[11] by combining radial PC MRI[10] and model-based image reconstruction[12] based on nonlinear inversion.[13] The approach allows for cross-sectional PC MRI at high spatio-temporal resolutions with only small latency between image acquisition and online display of results. However, three important aspects remain yet unresolved. First, the technique so far relied on independent image reconstructions for individual velocity components not taking full advantage of the redundancy inherent in multiple flow-encoding acquisitions. Second, the non-convex nature of the periodic phase-difference problem rendered the approach unstable for solutions near $\pm\pi$ and, thus, prone to artificial phase wraps especially for high degrees of data undersampling. And third, systematic phase offset errors induced by concomitant magnetic fields compromised quantitative velocity maps with different phase contributions for individual radial k-space lines. While the well-established Maxwell correction by Bernstein et al[14] is designed to compensate for these concomitant field effects, its original form is not applicable to PC MRI with undersampled radial trajectories. In contrast to Cartesian imaging with constant read gradients, radial read gradients continuously change (rotate), which is why corresponding concomitant fields characterized as Maxwell terms can vary for individual k-space lines. That is especially true for a timing-optimized[15] sequence[11] that merges radial imaging gradients with Cartesian flow-encoding gradients.

In this work, we address all these aspects by presenting a model-based image reconstruction that (1) jointly estimates all components of a velocity vector by combining up to four flow-encoding acquisitions, (2) suppresses artificial phase wraps by an additional penalty term and (3) incorporates a Maxwell correction that considers individual Maxwell terms for each radial k-space line.

2 | THEORY

2.1 | Signal model

Image reconstruction is formulated as a nonlinear inverse problem that is jointly solved for a complex image ρ, all coil profiles c_j and multiple velocity maps v_d representing the components of a velocity vector. As an extension of previous work on one-directional PC MRI[12] the forward model $F_{j,l}: x \mapsto y_{j,l}$ maps the unknowns $x = (\rho, v_1 \cdots v_D, c_1 \cdots c_N)$ to the raw data $y_{j,l}$ of the l^{th} flow-encoding dataset acquired by the j^{th} receiver coil.

$$F_{j,l}: x \mapsto P_l \,\mathrm{FT} \left\{ \rho \cdot \exp\left(i \sum_d E_{l,d}\, v_d \right) \cdot c_j \right\} \qquad (1)$$

where FT denotes the Fourier transform and P_l the sampling pattern. While ρ and c_j are complex, all velocity vector components v_d are real-valued such that different flow-encoding measurements are assumed to only differ in phase. The introduction of a velocity-encoding matrix E generalizes the basic 1D-flow model to a vector model of up to three dimensions. Here, E may be designed to reflect different flow-encoding strategies such as one-sided or balanced encoding.[16] In this work, the following encoding schemes are used:

$$\text{1D velocity vector: } E = \frac{1}{2} \cdot \begin{pmatrix} -1 \\ +1 \end{pmatrix} \qquad (2.1)$$

$$\text{2D velocity vector: } E = \frac{1}{2} \cdot \begin{pmatrix} -1 & +1 \\ +1 & +1 \\ +1 & -1 \end{pmatrix} \qquad (2.2)$$

$$\text{3D velocity vector: } E = \frac{1}{2} \cdot \begin{pmatrix} +1 & +1 & +1 \\ +1 & -1 & -1 \\ -1 & +1 & -1 \\ -1 & -1 & +1 \end{pmatrix}. \qquad (2.3)$$

2.2 | Radial Maxwell correction

According to Bernstein et al[14] the concomitant Maxwell terms for given gradient waveforms G_x, G_y and G_z and magnet-based coordinates x, y and z are well approximated by:

$$\phi^C(x,y,z) = \frac{\gamma}{2B_0}\int \left(G_x^2(t)+G_y^2(t)\right)z^2 + \frac{G_z^2(t)\left(x^2+y^2\right)}{4} - G_x(t)\,G_z(t)\,xz - G_y(t)\,G_z(t)\,yz\,\mathrm{d}t. \tag{3}$$

The purely quadratic spatial dependency can be summarized using the following dependency in image coordinates p and q:

$$\phi^C(p,q) = C_{pp}p^2 + C_{qq}q^2 + C_{pq}pq + C_p p + C_q q + C_0 \tag{4}$$

where linear and constant phase terms represent potential translations (off-center positions) and rotations of the imaging slice. In contrast to Cartesian sampling with a fixed read gradient and, thus, similar coefficients,[14] the Maxwell coefficients C_{pp}, C_{qq}, C_{pq}, C_p, C_q, and C_0 in general differ for individual radial k-space lines (i.e., spokes). For that reason, C_{pp} to C_0 are calculated in the pulse sequence for each spoke and each flow-encoding individually, as described in the Appendix. Afterward, all coefficients are stored along with the image raw data and passed on to the image reconstruction.

The Maxwell correction is performed during, i.e., as part of, the image reconstruction, because (1) a Maxwell correction as a preprocessing step that operates in k-space is not practical for undersampled data sets, and (2) neither a retrospective correction is reasonable, as it cannot address potential inter-spoke differences. Using the model-based PC formalism from above, the Maxwell phase maps $\phi_{l,s}^C$ are included in the signal model F. This way, the reconstruction directly estimates clean velocity maps v_d free of concomitant phase contributions, as the latter are explicitly modeled in the signal generation process:

$$F_{j,l}: x \mapsto \sum_s P_{l,s}\,\mathrm{FT}\left\{\rho\cdot\exp\left(i\,\phi_{l,s}^C\right)\cdot\exp\left(i\sum_d E_{l,d}\,v_d\right)\cdot c_j\right\} \tag{5}$$

Here, $\phi_{l,s}^C$ represents the calculated (and therefore known) phase contributions due to concomitant fields of the l^{th} flow-encoding step assumed to be constant along the s^{th} spoke, while the unknowns $x = (\rho, v_1\cdots v_D, c_1\cdots c_N)$ remain the same. This extension of Equation (1) includes single-spoke sampling operators $P_{l,s}$ and the summation along all spokes forming one frame. Consequently, the number of Fourier transforms increases and the computational cost of the iterative reconstruction scales with the number of spokes per frame.

As an alternative to a spoke-wise Maxwell correction, a less expensive frame-wise version based on a spoke-averaged approach is given by:

$$F_{j,l}: x \mapsto P_l\,\mathrm{FT}\left\{\rho\cdot\mu_l^C\cdot\exp\left(i\sum_d E_{l,d}\,v_d\right)\cdot c_j\right\} \tag{6}$$

where the complex map $\mu_l^C = \frac{1}{N_s}\sum_s \exp\left(i\,\phi_{l,s}^C\right)$ is obtained by averaging in advance (N_s being the number of spokes). Note that the magnitude of μ_l^C can be smaller than one to account for signal loss due to Maxwell phase cancellations. The corresponding derivative operator DF and its adjoint DF^H under Maxwell correction are given in the Appendix.

2.3 | Regularization

To jointly solve the nonlinear problem for all unkowns $x = (\rho, v_1\cdots v_D, c_1\cdots c_N)$ the iteratively regularized Gauss-Newton method is used which relies on several linearized subproblems around a current estimate x_n solved for an update $\mathrm{d}x$:

$$\underset{\mathrm{d}x}{\operatorname{argmin}} \left\| DF(x_n)\,\mathrm{d}x - (y - F(x_n)) \right\|_2^2 + \alpha_n \sum_i \left\| R_i\left(x_n + \mathrm{d}x - \lambda x_0\right) \right\|_2^2 \tag{7}$$

with corresponding normal equation:

$$\left(DF^H DF + \alpha_n \sum_i R_i^H R_i\right)\mathrm{d}x = DF^H\left(y - F(x_n)\right) - \alpha_n \sum_i R_i^H R_i\left(x_n - \lambda x_0\right). \tag{8}$$

Here, the regularization functions R_i act on $\mathrm{d}x$ and on the difference towards the previous frame x_0 (damped by a factor of $\lambda = 0.9$) to include temporal regularization. The regularization strength α_n is halved in each Newton iteration and coil smoothing is enforced by respective weighting in k-space as in Ref. 13. While previous work[12] relied on simple Tikhonov regularization for ρ and v using the identity matrix I as regularization function

$$R_1 = I \rightarrow \alpha_n \sum_i R_i^H R_i = \alpha_n R^H R = \alpha_n I. \tag{9}$$

This work proposes to add an initial smoothness constraint (ISC) in the first iterative steps to resolve the ambiguity of solutions near $\pm\pi$ and remove associated artificial phase wraps. In addition to the Tikhonov term ($R_1 = I$), image gradients in ρ and v_d are penalized ($R_2 = \sqrt{\beta_n}\,\nabla$) in early Newton iterations to favor smooth and thus unwrapped solutions of the periodic phase difference problem.

$$R_1 = I,\ R_2 = \sqrt{\beta_n}\nabla \rightarrow \alpha_n \sum_i R_i^H R_i = \alpha_n\left(I + \beta_n \nabla^H \nabla\right) = \alpha_n\left(I - \beta_n \Delta\right). \tag{10}$$

Here, the Laplace operator Δ is efficiently implemented as a small convolution kernel K_Δ:

$$K_{\Delta} = \begin{pmatrix} 0 & 1 & 0 \\ 1 & -4 & 1 \\ 0 & 1 & 0 \end{pmatrix}. \quad (11)$$

To avoid smoothing effects in final images, β_n drops to zero in the last iteration,

$$\beta_n = \begin{cases} 1 & \text{for } n < N \\ 0 & \text{for } n = N \end{cases} \quad (12)$$

where n denotes the index of the current step and N the total number of Newton iterations. Note that β_n determines the ratio of both regularization terms, while the overall regularization strength is determined by α_n. As in previous work,[12] α_n is initialized with 1 and decays with a factor of 2 for each successive iteration.

3 | METHODS

Experiments conducted to validate and evaluate the novel reconstruction techniques included simulations with a numerical phantom and experimental trials on a 3T MRI system (Magnetom Prisma fit, Siemens). The real-time PC sequence exploits asymmetric radial gradient echoes[17] and multi-directional flow sensitivity[11] using the balanced velocity-encoding strategies in Equations (2.1) to (2.3). All in vivo measurements were performed on young healthy volunteers (N = 5, 22–39 years) who provided written informed consent, according to the recommendations of the local ethics committee, prior to MRI.

In a preprocessing step, gradient delays were corrected by means of the RING method,[18] which was adapted to PC MRI by estimating common parameters for all flow encodings. All online calculations were done on a server (Supermicro SYS-1029GQ-TVRT) with four GPUs (NVIDIA V100 SXM2) and two CPUs (Intel Xeon Silver 4214) operating at 2.20 GHz with 192 GB DDR4-2933 MHz. If not noted otherwise, all image reconstructions used 7 Newton iterations.

3.1 | Numerical phantom

The method is validated on a numerical phantom[12] with known analytical Fourier transform. Three separate circles describing constant phase differences of $v = 80°$, 120°, and 160° in one, two, or three different velocity directions are created using two, three, or four individual velocity encodings, respectively. The radial raw data sets employed five projections (spokes) per frame for an image matrix size of 170 (undersampling factor: $170/5\,\frac{\pi}{2} = 53$). In addition to noise-free data sets, Gaussian white noise with an SD of 0.1 and 0.5 was added to the 10-channel k-space data. The receiver coils were simulated based on the Bio-Savart law and sinusoidal fitting.[19] Phase-difference maps were reconstructed without and with ISC according to (Equation 9) and (Equation 10), respectively. For all noise levels and both regularization techniques individual reconstructions were performed for up to 10 Newton iterations and analyzed for convergence of the quantitative phase-difference values by calculating root-mean-squared errors (RSME).

3.2 | Rotating disc and flow phantom

An in-house developed phantom, i.e., a rotating agarose disc of 16 cm diameter and 1.5 cm thickness, served for ground truth experiments. The disc was added to the set-up of an MR-compatible motion phantom[20] driven by a stepper motor with a controllable rotation frequency. Given an outer disc radius of $r_{out} = 8.0$ cm, an inner boundary of $r_{in} = 1.5$ cm and a rotation frequency of $f = 10.2\ \text{min}^{-1}$ the phantom provides a velocity range (as a function of distance from the disc's center) from $v = 1.6$ to 8.5 cm/s. Two-directional in-plane velocity mapping is performed with and without ISC, as well as with and without frame-wise and spoke-wise Maxwell corrections. RMSE values are compared for all reconstructions. In addition, a basic water-driven pulsatile flow phantom with tubing of 1-cm diameter was used for comparative experiments. Specific MRI parameters are listed in Table 1.

3.3 | In vivo experiments

In vivo velocimetry was performed on cervical cerebrospinal fluid (CSF) flow representing the slow flow regime ($v < 10$ cm/s) as well as in the aortic arch covering high blood velocities up to 150 cm/s. CSF flow was measured in a transversal plane at the cervical level C3 with through-plane flow sensitivity as in previous studies.[21] The same raw data was reconstructed with and without ISC. In addition, two-directional in-plane velocity maps were acquired in the median sagittal head section and image reconstructions were performed without, with frame-wise and with spoke-wise Maxwell correction. Region of interest (ROI) evaluations in areas of static tissue served for the assessment of velocity errors.

Blood velocities were quantified inside a cross-sectional imaging plane covering the aortic arch. All three velocity directions were encoded as given in Equation (2.3). Real-time PC MRI was performed without any assumptions regarding physiological periodicities (no gating, no data sorting, free breathing) rendering individual heartbeats

TABLE 1 Parameters for real-time PC MRI

	Numerical phantom	Flow phantom	Rotation phantom	CSF flow through-plane	CSF flow in-plane	Aortic blood flow
VENC [cm s^{-1}]	–	150	10	10	10	150
TE/TR [ms]	–	2.31/3.33	3.87/4.76	4.61/5.68	5.00/6.06	2.10/2.94
Flip angle [°]	–	10	10	10	10	10
Base resolution	170	192	128	256	192	178
Voxel size [mm^3]	–	$1 \times 1 \times 5$	$1.5 \times 1.5 \times 6$	$0.75 \times 0.75 \times 5$	$1.3 \times 1.3 \times 6$	$1.8 \times 1.8 \times 6$
Bandwidth [Hz pxl^{-1}]	–	840	1085	815	840	1220
Gradient amplitude [mT m^{-1}]	–	<34	<32	<26	<19	<28
Slew rate [T m^{-1} s^{-1}]	–	<141	<142	<116	<99	<140
Receiver channels	10	16	58	20	64	40
Spokes per frame	5	5	5	11	11	5
Velocity directions	1, 2, 3	2	2	1	2	3
Frames per second	–	20	14	8	5	17

and, thus, beat-to-beat variations accessible. Image reconstructions with and without ISC are compared, as well as reconstructions without, with frame-wise and with spoke-wise Maxwell correction. Again, areas of static tissue characterized velocity errors, while ROIs in the ascending and descending aorta served for a comparison of peak velocities. All MRI parameters are summarized in Table 1.

4 | RESULTS

4.1 | Initial smoothing constraint (ISC)

Figure 1 shows image reconstructions for the numerical phantom with Tikhonov regularization only (Equation 9) and additional ISC (Equation 10). For Newton iterations higher than 7, the results under simple Tikhonov regularization show phase wraps, even though the simulated phase differences are close to but still within the $[-\pi, \pi]$ interval. At the same time, the corresponding background phase reveals phase swaps of $\pm\pi$ in the very same pixels. The noise-free reconstructions and corresponding RMSE evaluation show such artificial phase wraps for Newton iterations larger than 8 (Figure 1, bottom). These findings hint at numerical instabilities for phase-difference values near $\pm\pi$, which are due to ambiguities in solution space imposed by phase periodicity. Higher noise levels and more Newton iterations (leading to a lower regularization strength α_n) amplify the effect.

Reconstructions with ISC reveal a more stable convergence, as neither phase wraps nor phase swaps (in the background phase) are observed. ISC resolves the solution's ambiguity by penalizing image gradients in early iterations favoring solutions free of spatial phase discontinuities in both ρ and v_d. ISC application in all but the last Newton iteration turns out to be optimal to achieve high-quality results. In particular, no image blurring and no noise reduction are observed as the last and decisive iteration remains unchanged. Similar results (not shown) are obtained for multi-directional velocity simulations.

Flow experiments shown in Figure 2 reveal artificial phase wraps for 7 Newton iterations. Here, partial volume effects at the vessel boundary seem to introduce phase swaps in the background phase. Using ISC, both phase swaps and correlated artificial phase wraps are avoided. The difference images point out that ISC barely compromises image sharpness and leaves the noise level unchanged. While artificial phase wraps for velocity values smaller than the velocity encoding (VENC) are resolved, true physical phase wraps in vessels with velocities higher than the VENC are nearly identical despite the use of ISC. Figure 3 underlines these findings. Table 2 summarizes the performance of ISC in terms of RMSE.

4.2 | Maxwell correction

Figure 3 shows the results of the rotating disc experiment demonstrating the performance of ISC and Maxwell correction. Next to the removal of artificial phase wraps by ISC, both in-plane velocity maps suffer from systematic velocity errors due to concomitant magnetic fields. Using the forward model (Equation 5), the velocity errors vanish, bringing the results obtained with ISC plus Maxwell correction into good agreement with the ground truth data as determined by disc dimensions and rotation frequency (see pink line plots and black reference line in Figure 3). Table 2 summarizes RMSE values for all reconstruction variants including the frame-wise Maxwell correction, which in this case yields nearly identical results (images not shown) to the spoke-wise approach.

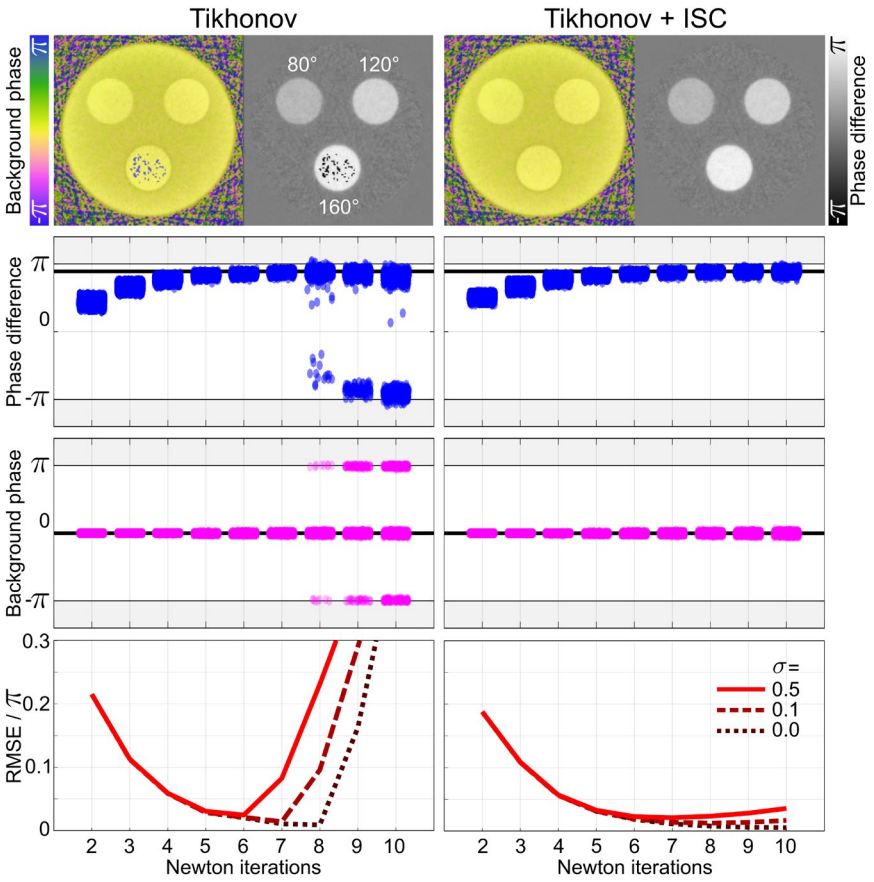

FIGURE 1 PC MRI reconstructions for a numerical phantom without and with ISC. Background-phase map and phase-difference map after 9 Newton iterations and noise level of 0.1 (top), phase difference values of pixels inside lowest circle as a function of Newton iterations (second row, blue), corresponding background-phase values (3rd row, pink), and root-mean-squared error for three different noise levels (bottom)

Figure 4 shows in-plane velocity maps from the two-directional CSF flow measurement in the cervical spinal canal. The upper part of Figure 5 illustrates corresponding Maxwell coefficients. The small VENC and, thus, large flow-encoding gradient moments lead to large phase offset errors in the reconstruction without Maxwell correction. Velocity errors of up to 5 cm/s in the static chin region corresponding to half the VENC are successfully removed both by the frame-wise and individual spoke-wise correction strategy. The only difference between both PC maps is narrowed down to small residual artifacts in the mouth region originating from minor inter-spoke differences of concomitant magnetic fields. While the frame-wise approach is computationally cheap (no extra FFTs), the spoke-wise Maxwell correction is capable of addressing the inter-spoke differences and, thus, results in cleaner velocity maps.

Not only for very low VENC values (10 cm/s) and correspondingly strong flow-encoding gradients, but also in the high VENC regime as used for aortic PC applications (150 cm/s) the concomitant field contributions at 3T can be significant. That is especially true using the radial PC sequence[11] with varying radial read gradients merged with Cartesian flow gradients and velocity encoding perpendicular to the B_0 field orientation. The lower part of Figure 5 illustrates the Maxwell coefficients for balanced three-directional velocity mapping at the human aortic arch. The six coefficients show a strong spoke-angle dependency and maximum values that indicate phase errors of up to 100° for a distance of 100 pixels from the isocenter. These significant phase errors become apparent in corresponding velocity maps, if not considered during image reconstruction. Figure 6 shows the velocity maps in all three flow directions after image reconstruction without, with frame-wise and spoke-wise Maxwell correction as given in Equations (1), (6) and (5), respectively. Severe image artifacts and phase-offset errors dominate the velocity maps obtained without correction. The frame-wise approach eliminates the static phase-offset errors while temporally oscillating artifacts remain. Their periodicity of five frames matches the periodicity of the turn-based sampling pattern chosen for real-time acquisitions and can be ascribed to inter-spoke differences in concomitant field contributions (Figure 5). The spoke-wise Maxwell correction successfully suppresses these phase errors and their temporal fluctuations as the forward model of this approach better describes the underlying physics. For the given example, the quality of the velocimetry method improves markedly, proving a spoke-wise treatment of Maxwell terms mandatory. ROI evaluations in the ascending and descending aorta located near the isocenter reveal no significant differences in peak velocities

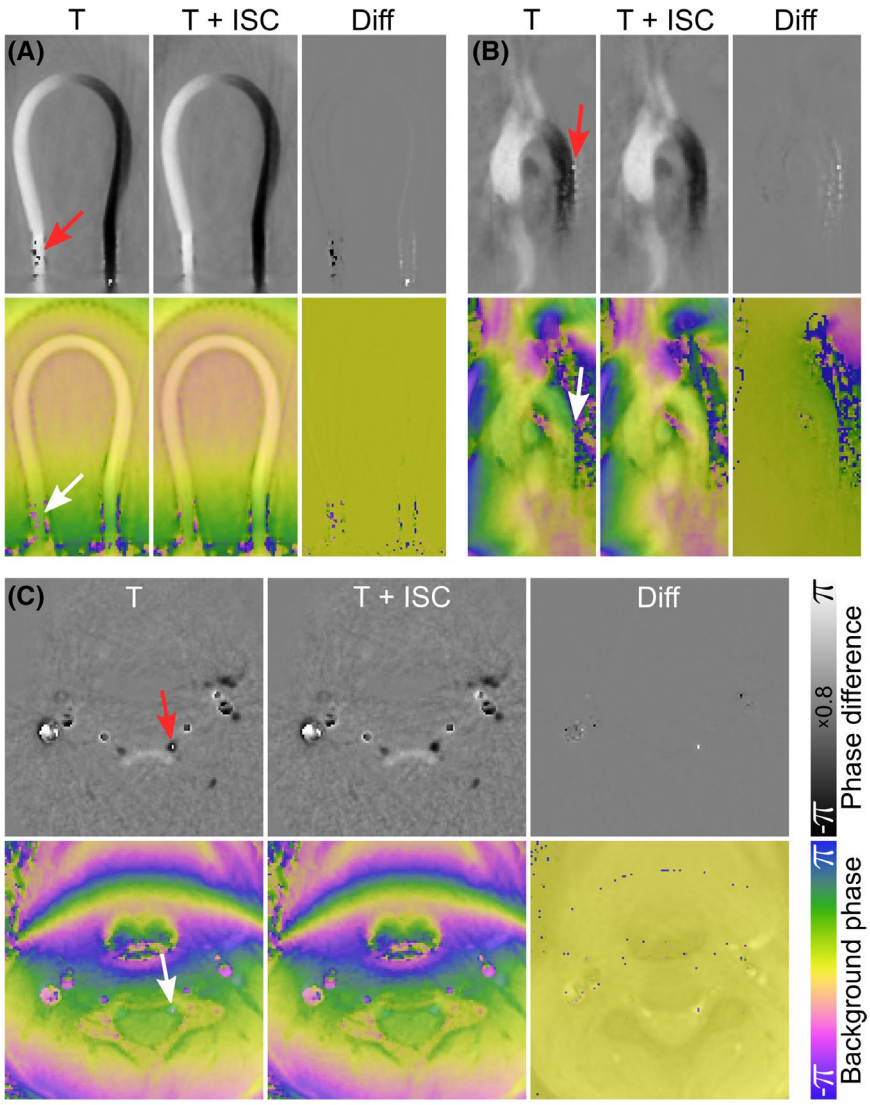

FIGURE 2 In-plane velocity maps and background phase of a flow phantom (A) and the aortic arch (B) as well as through-plane velocity maps of CSF and venous flow at spinal level C3 (C) using Tikhonov regularization only (T) and ISC plus their difference (Diff). Red and white arrows indicate artificial phase wraps and phase swaps, respectively

(see Supporting Information Figure S1, which is available online).

5 | DISCUSSION

This work presents a model-based image reconstruction for quantitative vectorial velocity mapping suited for real-time PC MRI. In comparison to previous work based on nonlinear inversion the novel technique includes (1) the extension to multi-directional flow, (2) a regularization-based suppression of artificial phase wraps, and (3) an integrated Maxwell correction for highly undersampled radial acquisitions that is able to compensate for potential inter-spoke differences of concomitant magnetic field contributions. These advances represent important steps to maintain the accuracy of the quantitative imaging tool under conditions of pronounced (radial) undersampling as required for highly accelerated PC MRI.

The ISC in early optimization steps successfully suppresses artificial phase wraps. These occur because the ambiguous solutions near $\pm\pi$ render the reconstruction prone to experimental inaccuracies, such as partial volume effects or noise, if exclusively the Tikhonov regularization is used. The additional penalty (ISC) for that reason is highly relevant in the presence of limited signal-to-noise ratio (SNR) caused by extreme data undersampling. The novel reconstruction favors a wrap-free solution with negligible image smoothing, as the extra penalty merely prevents the solution from too large phase discontinuities during the first steps of the iterative optimization. The algorithm was found to be insensitive to the respective weighting parameter $\beta = 1$ as a 10 times higher value led to nearly identical results (see Supporting Information Figure S2). That is because the additional penalty is switched off in the final optimization step, rendering the specific nature of the smoothing constraint little influential on the results. For the same reason, no significant difference was found in using a gradient penalty or an alternative Laplace penalty

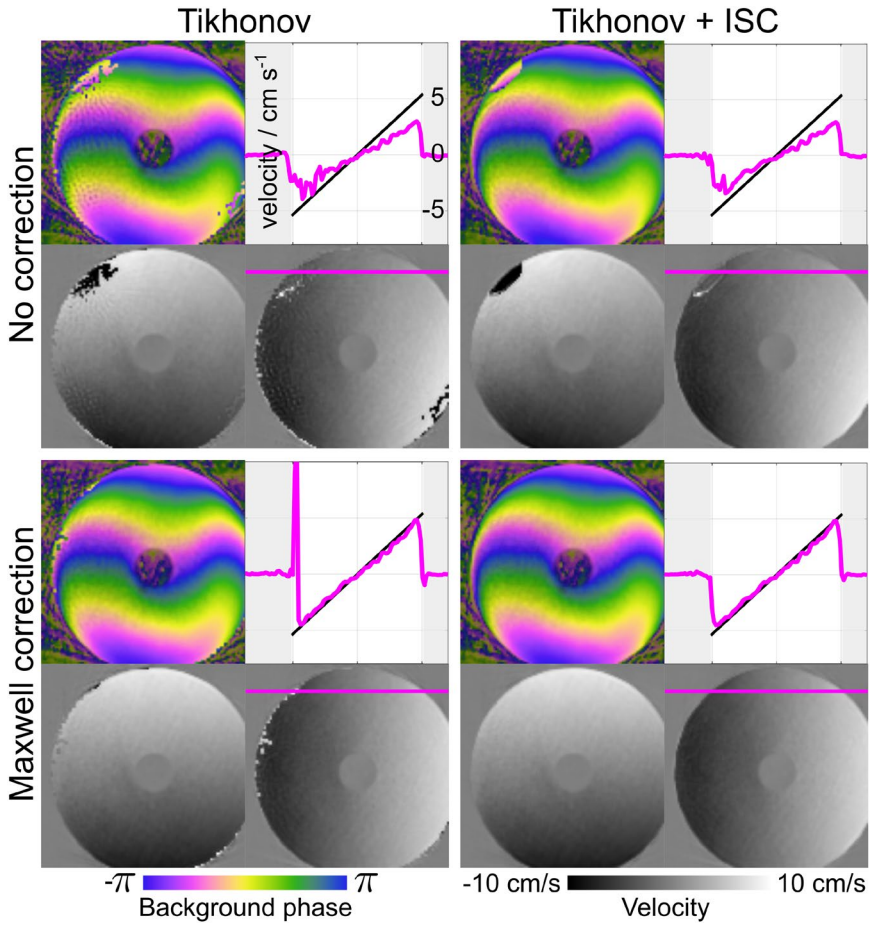

FIGURE 3 Two-directional in-plane velocity maps of a rotating disc reconstructed without (left) and with (right) ISC as well as without (top) and with (bottom) spoke-wise Maxwell correction. Only the combination of ISC and Maxwell correction results in a clean background phase and velocity maps that agree with the ground truth (pink and black lineplots)

TABLE 2 RMSE for the in-plane velocity maps of the rotation phantom

	Tikhonov	Tikhonov + ISC
No correction	1.85 cm s^{-1}	1.40 cm s^{-1}
Frame-wise Maxwell correction	1.00 cm s^{-1}	0.61 cm s^{-1}
Spoke-wise Maxwell correction	0.95 cm s^{-1}	0.60 cm s^{-1}

often proposed in other work on active phase unwrapping methods.[22,23] In contrast to related work[24] that unwraps velocity fields by penalizing its Laplacian in initial optimization steps, our approach only focuses on artificial phase wraps for velocities smaller than the VENC. Velocity aliasing for peak velocities higher than the VENC remains wrapped.

Related work on PC image reconstructions benefits from enforcing smooth background phases,[25] however, at the expense of computationally more expensive solvers. Our approach of enforcing a smooth complex image ρ (and, thus, a smooth background phase) comes with only minor additional computation costs. It is easily integrated into the existing Gauss-Newton algorithm, which is parallelized on a multi-GPU computer for fast online computations. Still, the current reconstruction speed of around four frames per second results in a latency of a few seconds between image acquisition and display.

This work further shows that an accelerated radial PC sequence can create significant concomitant field contributions even at a comparably high field strength of 3T. Especially low VENC values, fast gradient switching, high gradient amplitudes and velocity encoding perpendicular to B_0 favor the occurrence of pronounced velocity errors that render a Maxwell correction necessary. The proposed technique operates fully automated: it is integrated into the online image reconstruction pipeline and successfully compensates for Maxwell terms from undersampled radial acquisitions. In particular, inter-spoke differences are addressed by using a line-wise treatment of Maxwell terms. In contrast to previous corrections of concomitant field effects for spiral sampling,[26,27] where long readout times cause a time-dependent concomitant phase accumulation and associated image blurring, radial sampling as used here is sufficiently well treated by assuming constant concomitant phase contributions along each spoke. Unfortunately, the spoke-wise approach increases the computational demand, which scales with the number of spokes. In the current implementation and with only five spokes per frame, the reconstruction time approximately doubles.

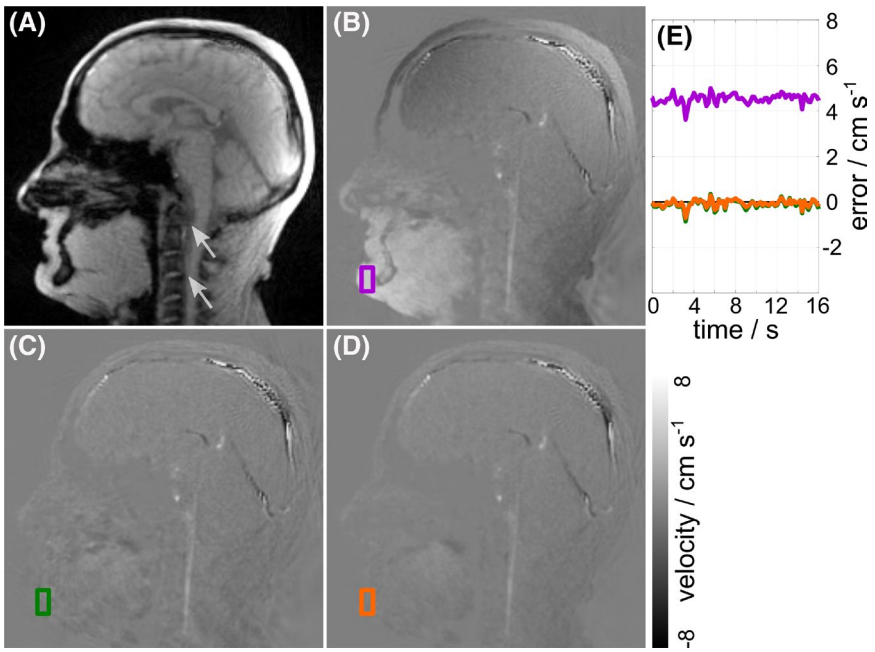

FIGURE 4 In-plane velocity maps for CSF quantification in midsagittal orientation. Magnitude image (A), velocity maps in feet-head direction without Maxwell correction (B), as well as with frame-wise (C) and spoke-wise (D) Maxwell correction, and ROI evaluation in static chin region (E). Arrows indicate the spinal canal with CSF flow of interest

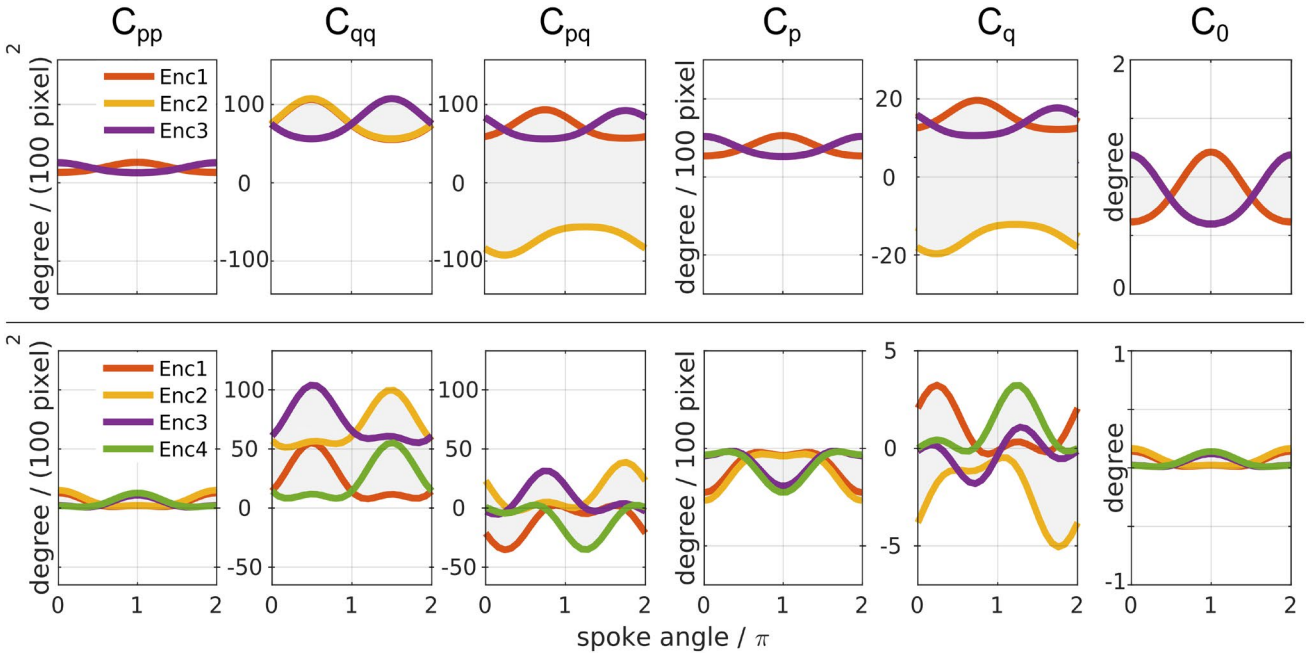

FIGURE 5 Maxwell coefficients according to Equation (4) as a function of spoke angle for two-directional velocity mapping of CSF flow (top) (Figure 4), and three-directional velocity mapping of the aortic arch (bottom) (Figure 6). Colors indicate different velocity-encoding steps

The alternative frame-wise, i.e., spoke-averaged, approach, on the other hand, comes at marginal costs, but is only applicable if inter-spoke differences of Maxwell terms can be neglected. The high sensitivity in sequence parameters such as echo time (TE), VENC, field of view (FOV), or image orientation, however, require individual decisions on what is acceptable for a specific imaging protocol. In general, the spoke-wise approach better describes the underlying physics. Previous publications on radial PC MRI either applied a retrospective correction of the background phase,[8] which can also compensate for eddy-current errors but not for potential inter-spoke differences in Maxwell terms, or did not comment on Maxwell correction and possibly neglected the influence of concomitant fields.[10,28] In certain scenarios, Maxwell terms are marginal or even vanish, e.g., for independent bipolar flow gradients and balanced velocity encoding. Usually, however, these scenarios go along with longer acquisition

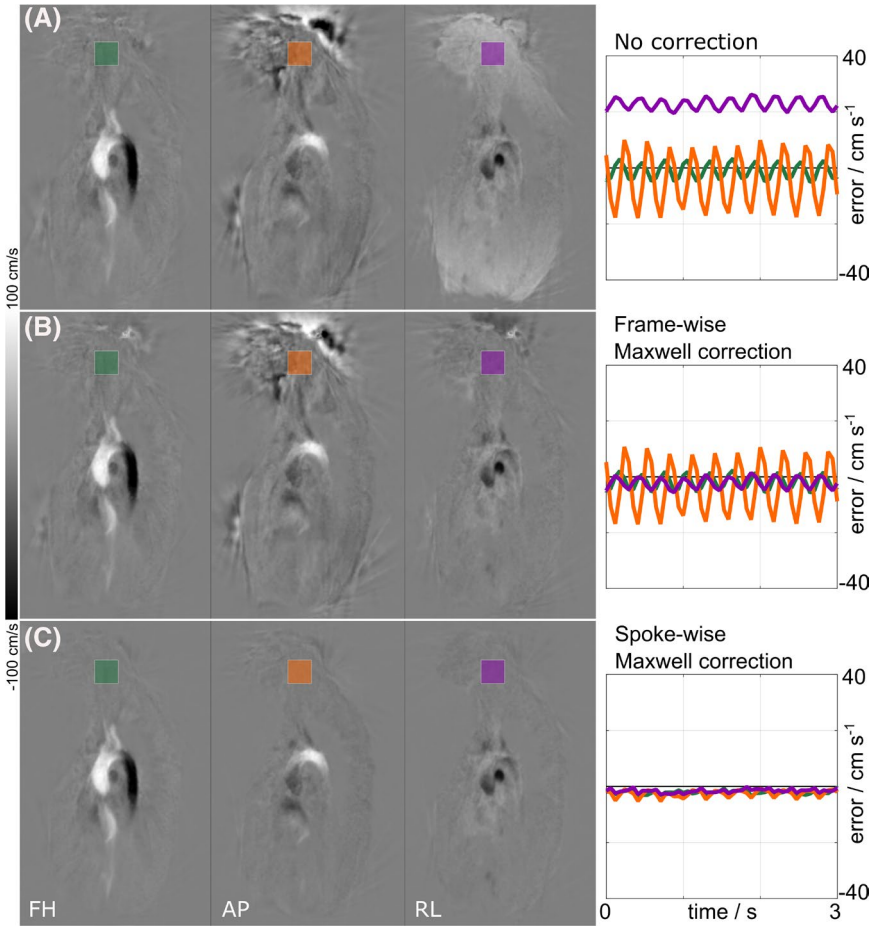

FIGURE 6 Three-directional velocity maps of the aortic arch without (A) as well as with (B) frame-wise and spoke-wise (C) Maxwell correction. Left, PC maps with flow sensitivity in feet-head (FH), anterior-posterior (AP), and right-left (RL) direction as well as (right) ROI evaluations in the static neck region revealing temporally fluctuating velocity errors

times. Limited to only a few examples, this work focused on very fast scenarios where a Maxwell correction is indispensable.

The calibration-less PC image reconstruction presented here builds on a very general model that may also be applied to volumetric imaging as in 4D flow.[29] The examples given in this work, however, are limited to cross-sectional imaging that lack access to complex 3D flow phenomena. Moreover, with 17 fps, i.e., 60 ms per three-directional acquisition, the cardiac examples not yet fulfill the clinical demand of 40 ms temporal resolution[30] to reliably resolve cardiac functions. Nevertheless, the multi-directional flow experiments point out the potential of the method in dealing with pronounced radial data undersampling as no gating or data sorting is required and true real-time movies are achieved (see Supporting Information Video S1).

Future methodological steps may include volumetric coverage by automated slice propagation[31] for motion-robust 3D imaging or the application to self-gated radial 4D flow data sets.[32] As all parts of the image reconstruction, including Maxwell correction, gradient delay correction, and coil estimation are performed online and fully automated for each frame, the image reconstruction presented here may be suited for imaging with interactive slice positioning. Presuming the latency of image acquisition to image display is minimized by sufficient computational speed, interactive multi-directional velocity mapping by real-time PC MRI may become a reality with variable slice positioning hitherto only achieved by Doppler sonography.

6 | CONCLUSIONS

Velocity vector reconstructions based on nonlinear inversion allow for high degrees of radial data undersampling and lay the foundation for vectorial velocity mapping in real time. The calibration-less reconstruction benefits from an ISC to avoid artificial phase wraps and from a radial Maxwell correction as part of the optimization process. Highly accelerated radial multi-directional PC MRI can provoke marked concomitant magnetic fields at 3T. Whether a spoke-wise treatment of Maxwell terms is required or only a computationally cheaper frame-wise approach depends on the MR parameters of individual applications.

ACKNOWLEDGMENT

Open access funding enabled and organized by ProjektDEAL.

ORCID

Jost M. Kollmeier https://orcid.org/0000-0002-7568-1221
Jens Frahm https://orcid.org/0000-0002-8279-884X

REFERENCES

1. Riederer SJ, Wright RC, Ehman RL, et al. Real-time interactive color flow MR imaging. *Radiology*. 1991;181:33-39.
2. Nayak KS, Pauly JM, Kerr AB, et al. Real-time color flow MRI. *Magn Reson Med*. 2000;43:251-258.
3. Nezafat R, Kellman P, Derbyshire JA, et al. Real-time blood flow imaging using autocalibrated spiral sensitivity encoding. *Magn Reson Med*. 2005;54:1557-1561.
4. Steeden JA, Atkinson D, Taylor AM, et al. Assessing vascular response to exercise using a combination of real-time spiral phase contrast MR and noninvasive blood pressure measurements. *J Magn Reson Imaging*. 2010;31:997-1003.
5. Traber J, Wurche L, Dieringer MA, et al. Real-time phase contrast magnetic resonance imaging for assessment of haemodynamics: from phantom to patients. *Eur Radiol*. 2016;26:986-996.
6. Yildiz S, Thyagaraj S, Jin N, et al. Quantifying the influence of respiration and cardiac pulsations on cerebrospinal fluid dynamics using real-time phase-contrast MRI. *J Magn Reson Imaging*. 2017;46:431-439.
7. Sun A, Zhao BO, Li Y, et al. Real-time phase-contrast flow cardiovascular magnetic resonance with low-rank modeling and parallel imaging. *J Cardiovasc Magn Reson*. 2017;19:1-13.
8. Haji-Valizadeh H, Feng L, Ma LE, et al. Highly accelerated, real-time phase-contrast MRI using radial k-space sampling and GROG-GRASP reconstruction: a feasibility study in pediatric patients with congenital heart disease. *NMR Biomed*. 2020;33:e4240.
9. Haji-Valizadeh H, Guo R, Kucukseymen S, et al. Highly accelerated free-breathing real-time phase contrast cardiovascular MRI via complex-difference deep learning. *Magn Reson Med*. 2021;86:804-819.
10. Joseph AA, Merboldt K-D, Voit D, et al. Real-time phase-contrast MRI of cardiovascular blood flow using undersampled radial fast low-angle shot and nonlinear inverse reconstruction. *NMR Biomed*. 2012;25:917-924.
11. Kollmeier JM, Tan Z, Joseph AA, et al. Real-time multidirectional flow MRI using model-based reconstructions of undersampled radial FLASH–A feasibility study. *NMR Biomed*. 2019;32:e4184.
12. Tan Z, Roeloffs V, Voit D, et al. Model-based reconstruction for real-time phase-contrast flow MRI: improved spatiotemporal accuracy. *Magn Reson Med*. 2017;77:1082-1093.
13. Uecker M, Hohage T, Block KT, et al. Image reconstruction by regularized nonlinear inversion—joint estimation of coil sensitivities and image content. *Magn Reson Med*. 2008;60:674-682.
14. Bernstein MA, Zhou XJ, Polzin JA, et al. Concomitant gradient terms in phase contrast MR: analysis and correction. *Magn Reson Med*. 1998;39:300-308.
15. Bernstein MA, Shimakawa A, Pelc NJ. Minimizing TE in moment-nulled or flow-encoded two-and three-dimensional gradient-echo imaging. *J Magn Reson Imaging*. 1992;2:583-588.
16. Pelc NJ, Bernstein MA, Shimakawa A, et al. Encoding strategies for three-direction phase-contrast MR imaging of flow. *J Magn Reson Imaging*. 1991;1:405-413.
17. Untenberger M, Tan Z, Voit D, et al. Advances in real-time phase-contrast flow MRI using asymmetric radial gradient echoes. *Magn Reson Med*. 2016;75:1901-1908.
18. Rosenzweig S, Christian H, Holme M, Uecker M. Simple auto-calibrated gradient delay estimation from few spokes using Radial Intersections (RING). *Magn Reson Med*. 2019;81:1898-1906.
19. Guerquin-Kern M, Lejeune L, Pruessmann KP, et al. Realistic analytical phantoms for parallel magnetic resonance imaging. *IEEE Trans Med Imaging*. 2012;31:626-636.
20. Frahm J, Schätz S, Untenberger M, et al. On the temporal fidelity of nonlinear inverse reconstructions for real- time MRI – the motion challenge. *Open J Med Imaging*. 2014;8:1-7.
21. Aktas G, Kollmeier JM, Joseph AA, et al. Spinal CSF flow in response to forced thoracic and abdominal respiration. *Fluids Barriers CNS*. 2019;16:10. https://doi.org/10.1186/s12987-019-0130-0
22. Loecher M, Schrauben E, Johnson KM, et al. Phase unwrapping in 4D MR flow with a 4D single-step laplacian algorithm. *J Magn Reson Imaging*. 2016;43:833-842.
23. Untenberger M, Hüllebrand M, Tautz L, et al. Spatiotemporal phase unwrapping for real-time phase-contrast flow MRI. *Magn Reson Med*. 2015;74:964-970.
24. Loecher M, Ennis DB. Velocity reconstruction with nonconvex optimization for low-velocity-encoding phase-contrast MRI. *Magn Reson Med*. 2018;80:42-52.
25. Ong F, Cheng JY, Lustig M. General phase regularized reconstruction using phase cycling. *Magn Reson Med*. 2018;80:112-125.
26. King KF, Ganin A, Zhou XJ, Bernstein MA. Concomitant gradient field effects in spiral scans. *Magn Reson Med*. 1999;41:103-112.
27. Chen W, Sica CT, Meyer CH. Fast conjugate phase image reconstruction based on a Chebyshev approximation to correct for B0 field inhomogeneity and concomitant gradients. *Magn Reson Med*. 2008;60:1104-1111.
28. Gu T, Korosec FR, Block WF, et al. PC VIPR: a high-speed 3D phase-contrast method for flow quantification and high-resolution angiography. *Am J Neuroradiol*. 2005;26:743-749.
29. Markl M, Frydrychowicz A, Kozerke S, et al. 4D flow MRI. *J Magn Reson Imaging*. 2012;36:1015-1036.
30. Dyverfeldt P, Bissell M, Barker AJ, et al. 4D flow cardiovascular magnetic resonance consensus statement. *J Cardiovasc Magn Reson*. 2015;17:1-19.
31. Voit D, Kalentev O, Zalk M, et al. Rapid and motion-robust volume coverage using cross-sectional real-time MRI. *Magn Reson Med*. 2020;83:1652-1658.
32. Ma LE, Yerly J, Piccini D, et al. 5D flow MRI: a fully self-gated, free-running framework for cardiac and respiratory motion–resolved 3D hemodynamics. *Radiology: Cardiothoracic Imaging*. 2020;2:e200219.

SUPPORTING INFORMATION

Additional supporting information may be found in the online version of the article at the publisher's website.

FIGURE S1 Velocity time curves obtained by ROI evaluation in the ascending (blue) and descending aorta (red). As these regions are located close to the iso-center, no significant differences in mean peak velocity (±SD) are observed without or with radial Maxwell correction

FIGURE S2 In-plane velocity maps for the flow phantom (top) and the aortic arch (middle, bottom) for different strengths (β) of the initial smoothing constraint (ISC). The right-most column ($\beta = 1^*$) corresponds to a Laplace penalty (instead of image gradient penalty). Red arrows indicate artificial phase wraps

VIDEO S1 Real-time MRI movie of three-directional velocity maps of the aortic arch at 17 fps (top) without as well as with (middle) frame-wise and (bottom) spoke-wise Maxwell correction

How to cite this article: Kollmeier JM, Kalentev O, Klosowski J, Voit D, Frahm J. Velocity vector reconstruction for real-time phase-contrast MRI with radial Maxwell correction. *Magn Reson Med*. 2022;87:1863–1875. doi:10.1002/mrm.29108

APPENDIX

Coefficients for Maxwell correction

To calculate the phase-error maps ϕ^C induced by concomitant magnetic fields, we initially follow Bernstein et al[14] using the four coefficients A to D

$$A = \frac{\gamma}{2B_0}\int G_x^2(t) + G_y^2(t)\,\mathrm{d}t$$

$$B = \frac{\gamma}{8B_0}\int G_z^2(t)\,\mathrm{d}t$$

$$C = -\frac{\gamma}{2B_0}\int G_x(t)\,G_z(t)\,\mathrm{d}t$$

$$D = -\frac{\gamma}{2B_0}\int G_y(t)\,G_z(t)\,\mathrm{d}t$$

Using these, we obtain ϕ^C as a function of magnet-based coordinates x, y,z

$$\phi^C(x,y,z) = Az^2 + B\left(x^2+y^2\right) + Cxz + Dyz$$

To recover the correct coordinates in each pixel of the image, however, in this notation, the image orientation defined by the rotation matrix Γ, the distance to the iso-center $\vec{\Delta}$ as well as the pixel size ps must be known and stored in addition to the coefficients A to D. Instead of extracting all these variables for the image reconstruction, we use the following formalism instead to condense the number of variables to a minimum:

$$\phi^C(p,q) = C_{pp}p^2 + C_{qq}q^2 + C_{pq}pq + C_p p + C_q q + C_0$$

By using the image coordinates p and q (pixel integers), the novel coefficients C_{pp} to C_0 now contain the information on imaging-plane position and orientation implicitly. These coefficients are calculated in the MR sequence for each k-space line as follows:

$$C_{pp} = ps^2\left(A\Gamma_{3,1}^2 + B\left(\Gamma_{1,1}^2+\Gamma_{2,1}^2\right) + C\Gamma_{1,1}^2\Gamma_{3,1}^2 + D\Gamma_{2,1}^2\Gamma_{3,1}^2\right)$$

$$C_{qq} = ps^2\left(A\Gamma_{3,2}^2 + B\left(\Gamma_{1,2}^2+\Gamma_{2,2}^2\right) + C\Gamma_{1,2}^2\Gamma_{3,2}^2 + D\Gamma_{2,2}^2\Gamma_{3,2}^2\right)$$

$$\begin{aligned}C_{pq} = ps^2\big(&2A\Gamma_{3,1}\Gamma_{3,2} + B\left(\Gamma_{1,1}\Gamma_{1,2}+\Gamma_{2,1}\Gamma_{2,2}\right)\\ &+C\left(\Gamma_{1,1}\Gamma_{3,2}+\Gamma_{1,2}\Gamma_{3,1}\right) + D(\Gamma_{2,1}\Gamma_{3,2}+\Gamma_{2,2}\Gamma_{3,1})\big)\end{aligned}$$

$$\begin{aligned}C_p = ps\big(&2A\Gamma_{3,1}\Delta_3 + 2B\left(\Gamma_{1,1}\Delta_1+\Gamma_{2,1}\Delta_2\right)\\ &+C\left(\Gamma_{1,1}\Delta_3+\Gamma_{3,1}\Delta_1\right) + D(\Gamma_{2,1}\Delta_3+\Gamma_{3,1}\Delta_2)\big)\end{aligned}$$

$$\begin{aligned}C_q = ps\big(&2A\Gamma_{3,2}\Delta_3 + 2B\left(\Gamma_{1,2}\Delta_1+\Gamma_{2,2}\Delta_2\right)\\ &+C\left(\Gamma_{1,2}\Delta_3+\Gamma_{3,2}\Delta_1\right) + D(\Gamma_{2,2}\Delta_3+\Gamma_{3,2}\Delta_2)\big)\end{aligned}$$

$$C_0 = A\Delta_3^2 + B\left(\Delta_1^2+\Delta_2^2\right) + C\Delta_1\Delta_3 + D\Delta_2\Delta_3$$

Derivative operators under spoke-wise Maxwell correction

Next to the forward operator F given in Equation (5), its Fréchet derivative DF is required to linearize the signal model:

$$DF_{j,l}(x)\begin{pmatrix} \mathrm{d}\rho \\ \mathrm{d}v_1 \\ \vdots \\ \mathrm{d}v_D \\ \mathrm{d}c_1 \\ \vdots \\ \mathrm{d}c_N \end{pmatrix} = \frac{1}{N_s}\sum_s^{N_s} P_{l,s}\,\mathrm{FT}\left\{\exp\left(i\,\phi_{l,s}^{C}\right)\cdot\exp\left(i\sum_d E_{l,d}\,v_d\right)\cdot\left(c_j\mathrm{d}\rho+\rho\mathrm{d}c_j+\sum_d \rho c_j i E_{l,d}\mathrm{d}v_d\right)\right\}$$

The Gauss-Newton method further employs its adjoint DF^H mapping $\mathrm{d}y$ to $\mathrm{d}x$:

$$DF^H(x)\begin{pmatrix} \mathrm{d}y_{1,1} \\ \vdots \\ \mathrm{d}y_{N,1} \\ \vdots \\ \mathrm{d}y_{1,D+1} \\ \vdots \\ \mathrm{d}y_{N,D+1} \end{pmatrix} = \begin{pmatrix} \sum_j c_j^*\left[\sum_l \mu_l^*\cdot\exp\left(-i\sum_d E_{l,d}\,v_d\right)\cdot\mathrm{FT}^{-1}\left\{P_l^H\mathrm{d}y_{j,l}\right\}\right] \\ \mathrm{Re}\left\{\sum_j \rho^*\cdot c_j^*\left[\sum_l \mu_l^*\cdot i\cdot E_{l,1}\cdot\exp\left(-i\sum_d E_{l,d}\,v_d\right)\cdot\mathrm{FT}^{-1}\left\{P_l^H\mathrm{d}y_{j,l}\right\}\right]\right\} \\ \vdots \\ \mathrm{Re}\left\{\sum_j \rho^*\cdot c_j^*\left[\sum_l \mu_l^*\cdot i\cdot E_{l,D}\cdot\exp\left(-i\sum_d E_{l,d}\,v_d\right)\cdot\mathrm{FT}^{-1}\left\{P_l^H\mathrm{d}y_{j,l}\right\}\right]\right\} \\ \sum_l \rho^*\cdot\mu_l^*\cdot\exp\left(-i\sum_d E_{l,d}\,v_d\right)\cdot\mathrm{FT}^{-1}\left\{P_l^H\mathrm{d}y_{1,l}\right\} \\ \vdots \\ \sum_l \rho^*\cdot\mu_l^*\cdot\exp\left(-i\sum_d E_{l,d}\,v_d\right)\cdot\mathrm{FT}^{-1}\left\{P_l^H\mathrm{d}y_{N,l}\right\} \end{pmatrix}$$